

# Drop race: How electrostatic forces influence drop motion

**Xiaomei Li**

Max Planck Institute for Polymer Research <https://orcid.org/0000-0003-3362-148X>

**Pravash Bista**

Max Planck Institute for Polymer Research <https://orcid.org/0000-0003-3807-1704>

**Amy Stetten**

Max Planck Institute for Polymer Research

**Henning Bonart**

Max Planck Institute for Polymer Research

**Maximilian Schür**

Technische Universität Darmstadt <https://orcid.org/0000-0003-0849-0799>

**Steffen Hardt**

Technische Universität Darmstadt

**Francisco Bodziony**

Technische Universität Darmstadt

**Holger Marschall**

Technische Universität Darmstadt

**Alexander Saal**

Max Planck Institute for Polymer Research

**Xu Deng**

University of Electronic Science and Technology of China <https://orcid.org/0000-0002-9659-0417>

**Rüdiger Berger**

Max Planck Institute for Polymer Research <https://orcid.org/0000-0002-4084-0675>

**Stefan Weber**

Max Planck Institute for Polymer Research

**Hans-Jürgen Butt** (✉ [butt@mpip-mainz.mpg.de](mailto:butt@mpip-mainz.mpg.de))

Max Planck Institute for Polymer Research <https://orcid.org/0000-0001-5391-2618>

---

## Article

**Keywords:** hydrophobic surfaces, electrostatic forces, low-permittivity substrates

**Posted Date:** August 30th, 2021

**DOI:** <https://doi.org/10.21203/rs.3.rs-737950/v1>

**License:**  This work is licensed under a Creative Commons Attribution 4.0 International License.

[Read Full License](#)

---

**Version of Record:** A version of this preprint was published at Nature Physics on April 14th, 2022. See the published version at <https://doi.org/10.1038/s41567-022-01563-6>.

1

## Drop race:

2

### How electrostatic forces influence drop motion



3

4 Xiaomei Li<sup>1</sup>, Pravash Bista<sup>1</sup>, Amy Stetten<sup>1</sup>, Henning Bonart<sup>1,2</sup>, Maximilian T. Schür<sup>2</sup>, Steffen  
5 Hardt<sup>2</sup>, Francisco Bodziony<sup>3</sup>, Holger Marschall<sup>3</sup>, Alexander Saal<sup>1</sup>, Xu Deng<sup>4</sup>, Rüdiger Berger<sup>1</sup>,  
6 Stefan Weber<sup>1\*</sup>, Hans-Jürgen Butt<sup>1\*</sup>

7 <sup>1</sup> Max Planck Institute for Polymer Research, Ackermannweg 10, 55128 Mainz, Germany

8 <sup>2</sup> Institute for Nano- and Microfluidics, Technische Universität Darmstadt, Alarich-Weiss-  
9 Straße 10, 64287 Darmstadt, Germany

10 <sup>3</sup> Computational Multiphase Flows, Technische Universität Darmstadt, Alarich-Weiss-Straße  
11 10, 64287 Darmstadt, Germany

12 <sup>4</sup> Institute of Fundamental and Frontier Sciences, University of Electronic Science and  
13 Technology of China, Chengdu, China.

#### 14 **Abstract**

15 Water drops sliding down inclined planes are an everyday phenomenon and are important in  
16 many technical applications. Previous understanding is that the motion is mainly dictated by  
17 viscous and capillary forces. Here we demonstrate that, in addition to these forces, drops on  
18 hydrophobic surfaces are affected by self-generated electrostatic forces. In a novel approach  
19 to determine forces on moving drops we imaged their trajectory when sliding down a tilted  
20 surface and apply the equation of motion. We found that drop motion on low-permittivity  
21 substrates is significantly influenced by electrostatic forces. Sliding drops deposit a negative  
22 charge on the surface, which interact with the positively charged drops. We derive an  
23 analytical model to describe the force and validate it by numerical computations. The results

24 indicate how to describe and facilitate drop motion in applications, such as in microfluidics,  
25 water management on car surfaces, and the creation of sliding drop electrical generators.

26

27 Water drops sliding over surfaces is a common phenomenon<sup>1-3</sup>. The lateral adhesion of drops  
28 can be nuisance; for example, the struggle to keep textiles, feathers, or fur dry, to keep drops  
29 from sticking in microfluidics, or to keep window screens and glasses clear in the rain<sup>4-7</sup>. In  
30 other applications, a resistance of sessile drops to sliding motion is essential, for example in  
31 coating, painting, deposition of insecticides and herbicides, or in flotation<sup>8,9</sup>. Recently, the  
32 motion of drops has attracted attention because sliding water drops have been proposed to  
33 generate electricity<sup>10-17</sup>. Still, a full description of drops' trajectories remains elusive.

34 In accepted literature, the motion of drops is assumed to be determined by capillary and  
35 viscous forces<sup>1-3,9,18-20</sup>. The capillary force<sup>7,21</sup>,

$$36 \quad F_c = w\gamma k(\cos \Theta_r - \cos \Theta_a) \quad (1)$$

37 originates from the difference of the advancing  $\Theta_a$  and the receding contact angles  $\Theta_r$ . Here,  
38  $w$  is the width of the contact area of the drop,  $\gamma$  is the surface tension of the liquid and  $k \approx 1$   
39 is a geometrical factor, which depends on the detailed shape of the drop<sup>22-24</sup>. In general, the  
40 contact angles and the width are sensitive to velocity.

41 Viscous force arises because of viscous hydrodynamic flow within the drop. The viscous force  
42 of a sliding drop is commonly split in two components. Both are, to first order, proportional  
43 to the slide velocity  $U$ . One component comes from the viscous dissipation in the bulk,  $F_b$ , and  
44 the other from the wedge of the drop,  $F_w$ <sup>24-26</sup>. Bulk viscous dissipation can be approximated  
45 by (Supporting information, SI1),

$$46 \quad F_b \approx \eta \frac{\pi l w}{2H} U \quad (2)$$

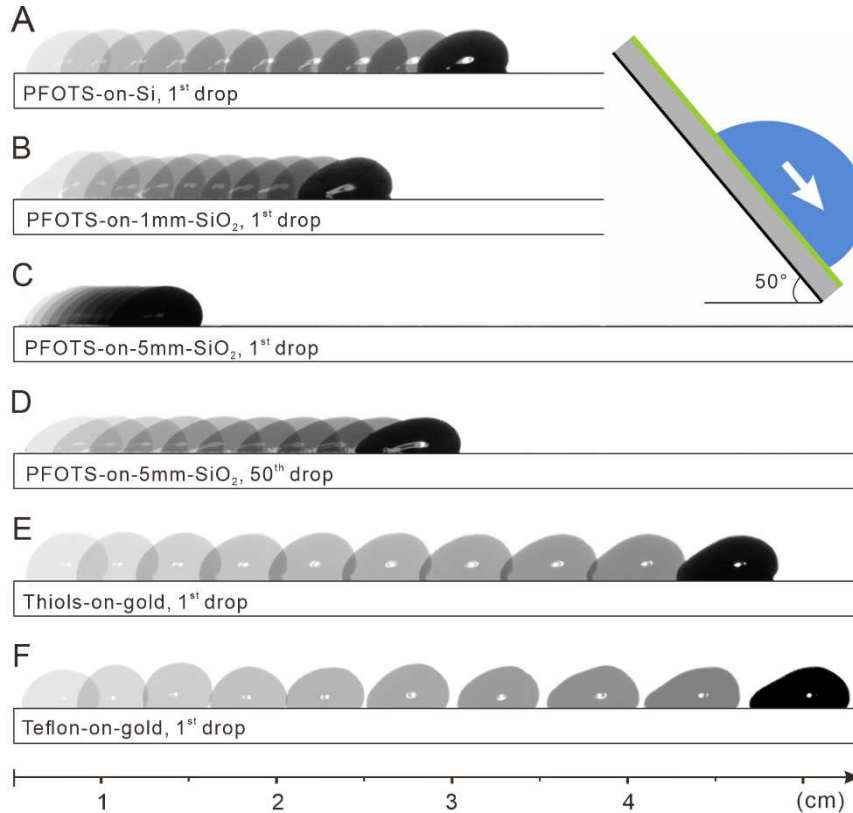
47 Here,  $\eta$  denotes the dynamic viscosity of the liquid,  $l$  is the length of the drop, and  $H$  is its  
48 height. Viscous dissipation in the wedge is dominated by flow close to the contact line at a  
49 length scale  $\leq 10 \mu\text{m}$ . Since we observe contact angles at a larger length scale, it would  
50 manifest itself in a change of the macroscopic contact angles and is already included in Eq. (1).

51 Here we demonstrate by a simple tilted plate experiment that the motion of drops cannot be  
52 accurately predicted by these two forces. In a tilted plate experiment, a defined gravitational  
53 force  $F_g = mg \sin \alpha$  is acting in lateral direction<sup>20,26-32</sup>. Here,  $m$  is the mass of the drop,  $g=9.81$   
54  $\text{m/s}^2$  is the standard acceleration of gravity, and  $\alpha$  is the tilt angle.

55 Interesting results were observed for water drops sliding on different substrates. A drop  
56 sliding on a silicon wafer coated with perfluorooctadecyltrichlorosilane (PFOTS) moves  
57 relatively quickly; in our drop race at  $50^\circ$  tilt the drop covered a distance of 2.5 cm within 100  
58 ms (Figure 1A). In contrast, on a PFOTS-coated 1 mm thick  $\text{SiO}_2$  plate (PFOTS-on-1mm- $\text{SiO}_2$ ) a  
59 water drop only reached a distance of 1.7 cm in 100 ms (Figure 1B). On a 5 mm thick  $\text{SiO}_2$  plate  
60 (PFOTS-on-5mm- $\text{SiO}_2$ ) the drop moved only few millimetres (Figure 1C). In addition, for series  
61 of drops, sliding speeds become dependent on the drop number and thus their history. In the  
62 above examples, we showed the respective first drops of a series. Subsequent drops have a  
63 different velocity. For example, the 50<sup>th</sup> drop sliding down PFOTS-5mm- $\text{SiO}_2$  is faster than the  
64 first drop (Figure 1D). Although the surface chemistry of the three samples is identical and one

65 expects similar capillary and viscous forces, the sliding speed of drops varied by more than a  
 66 factor two.

67 We observed even faster drop motion on a gold surface coated with a monolayer of  
 68 perfluorodecanethiol (Figure 1E) and Teflon films on gold (Figure 1F), although the surface  
 69 chemistry is comparable to PFOTS-coated surfaces. This simple experiment already  
 70 demonstrates that there is an important contribution missing in the description of drop  
 71 motion.



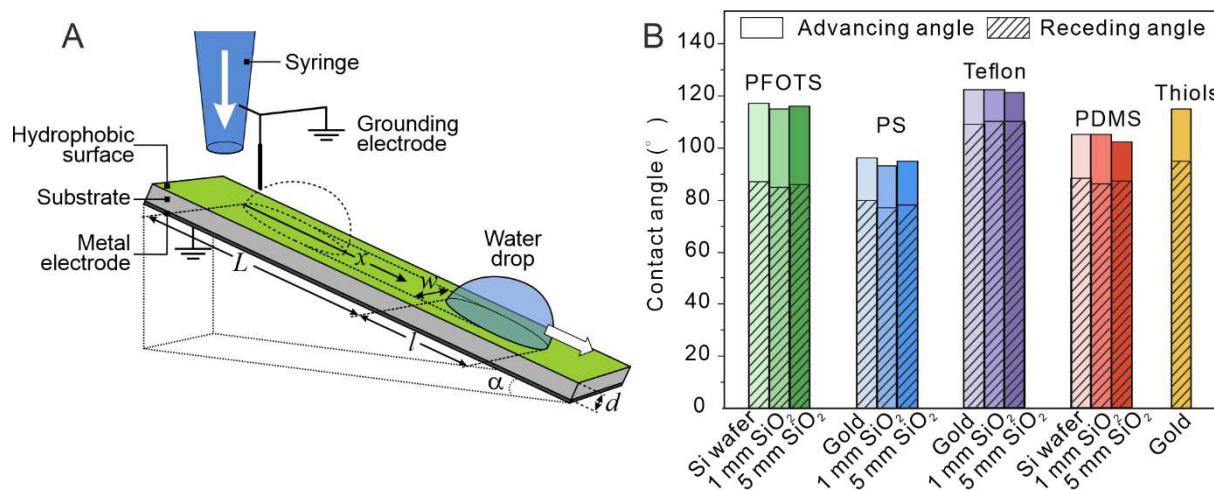
72  
 73 **Figure 1.** 33  $\mu\text{L}$  water drops sliding down a plate tilted by 50° after detaching from a grounded  
 74 electrode and imaged every 10 ms with a side-view camera.

75 It is known that on bulk Teflon samples, fluorinated insulators, and superhydrophobic  
 76 surfaces, sliding water drops deposit negative electric charges, while the drops acquire a  
 77 positive charge<sup>11,12,14,33-38</sup>. Surface charges generate an electric field in the air above the  
 78 surface. A charge  $q$  on top of an infinitely extending dielectric half space with a relative  
 79 permittivity  $\epsilon_S$  generates an electric field

80 
$$E = \frac{q}{2\pi\epsilon_0(\epsilon_S+1)r^2}. \tag{3}$$

81 Here,  $\epsilon_0$  is the vacuum permittivity and  $r$  is the distance from the charge. This electric field  
 82 causes a Coulomb force on a charged drop. Thus, any electrostatic force on a dielectric surface  
 83 scale with  $1/(1 + \epsilon_S)$ .

84 Given the importance of sliding drops in our daily lives, we address the following questions:  
 85 Which extra forces determine drop trajectories? Are the extra forces electrostatic in origin?  
 86 Can they be measured quantitatively? Why and how does the substrate influence drop  
 87 motion? Why is the motion of a drop influenced by previous drops? To answer these question  
 88 and measure directly forces acting on moving drops we develop a new method to analyse  
 89 titled plate experiments.

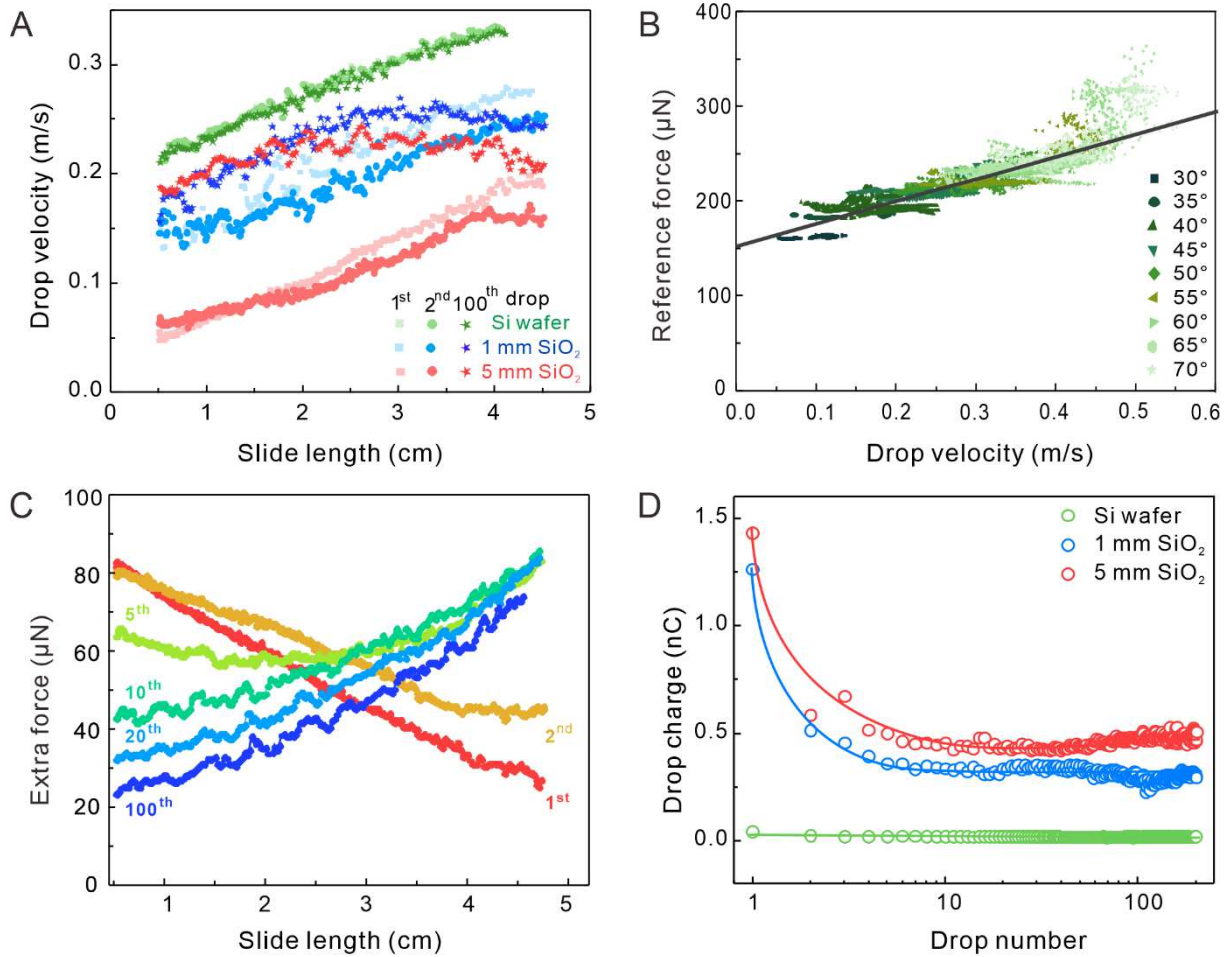


90  
 91 **Figure 2.** (A) Schematic of the experimental setup. (B) Hydrophobic samples studied. The  
 92 “static” advancing and receding contact angles  $\theta_a^0$  and  $\theta_r^0$  were measured with sessile water  
 93 drops during slowly inflating and deflating and imaging in side view (SI3).

94 We prepared smooth, hydrophobic surfaces with receding and advancing contact angles  
 95 ranging between 77–110° and 93–122°, respectively (Figure 2B, SI3). All surfaces had a  
 96 roughness  $rms \leq 1$  nm as determined by scanning force microscopy (SI4). In order to find out  
 97 how strong electrostatic forces are, we varied the substrate and its thickness  $d$  with respect  
 98 to a grounded metal back-electrode. We chose SiO<sub>2</sub> plates ( $\epsilon_S = 3.9$ ) as a low permittivity  
 99 substrate and Si wafers with only a natural oxide layer as a high permittivity sample ( $\epsilon_S =$   
 100 11.7). In the presence of the grounded metal back-electrode, the field is screened by image  
 101 charges. The distance to the grounded metal layer defines the screening length.

102 To describe the results and analysis, we first concentrate on PFOTS-coated samples. For  
 103 PFOTS-on-Si, the first, second, and subsequent drops showed similar velocity profiles (Figure  
 104 3A, green symbols). In contrast to common expectation, on 1 mm and on 5 mm thick SiO<sub>2</sub>  
 105 substrates (Figure 3A, blue and red symbols), velocity profiles of the first, second, and  
 106 subsequent drops were distinctly different, although all samples have similar contact angles.  
 107 Firstly, velocities tended to be lower on SiO<sub>2</sub> than on the silicon wafer. Secondly, often rather  
 108 complex traces occurred. These traces were, however, systematic and reproducible. For  
 109 example, on PFOTS-on-5mm-SiO<sub>2</sub> the first drops showed a monotonically increasing velocity  
 110 (Figure 3A, red squares). For drop number  $n \geq 50$  (Figure 3A, red stars) the velocity first  
 111 increased but after 3 cm slide distance, it decreased again.

112 We draw two conclusions: First, drop motion is not only determined by capillary and viscous  
 113 forces. Second, there is a fundamental difference between static and dynamic wetting. The  
 114 static shape of a drop is largely determined by the properties of the topmost 1 nm of the  
 115 surface; the substrate underneath has little influence. In contrast, the dynamic properties such  
 116 as the sliding speed are influenced by the substrate down to a thickness of the order of 1 mm.



117  
 118 **Figure 3.** Results obtained with 33  $\mu\text{L}$  water drops on PFOTS-coated samples. (A) Velocity-  
 119 versus-slide length for PFOTS-on-Si (green symbols), 1 mm (blue) and 5 mm  $\text{SiO}_2$  (red) sliding  
 120 down at an inclination of  $\alpha = 50^\circ$ . See SI5 for other tilt angles. (B) Reference forces measured  
 121 on 4 samples of PFOTS-on-Si. Fitting the results for  $U \leq 0.4 \text{ m/s}$  (grey lines) led to  $F_r =$   
 122  $156 \mu\text{N} + 218 \frac{\mu\text{Ns}}{\text{m}} \cdot U$ . (C) Extra forces acting on the 1<sup>st</sup>, 2<sup>nd</sup>, 5<sup>th</sup>, 10<sup>th</sup>, 20<sup>th</sup>, and 100<sup>th</sup> drop  
 123 sliding down 50° tilted PFOTS-on-5mm-SiO<sub>2</sub>. Forces were calculated with Eq. (4) with PFOTS-  
 124 on-Si as a reference. (D) Measured drop charge-versus-drop number on PFOTS-coated samples.  
 125 Results were measured at 50° tilt, 1.5 s intervals between deionized water drops of 45  $\mu\text{L}$   
 126 volume after 4 cm slide length. Lines are there to guide the eye. Details in SI10.

127 To quantify the extra force, we analyse the equation of motion of a drop:

128 
$$m^* \frac{dU}{dt} = mg \sin \alpha - F_r(U) - F_e^n(U, L) \quad (4)$$

129 In the acceleration term,  $m^* \frac{dU}{dt}$ , we take into account rolling components in drops-motion  
130 <sup>1,9,20,32,39,40</sup>. Therefore, we used the effective mass  $m^*$ , which was determined by direct  
131 numerical diffuse interface simulations of the flow pattern inside sliding drops (SI6). These  
132 simulations gave an estimate of  $m^*/m=1.05$  as a good mean value for the velocity range  
133 covered by our experiments.

134 All forces acting on the drop in the absence of electrostatic effects are summarized in the  
135 reference force,  $F_r(U)$ . The reference force depends on the velocity  $U$  but not on the slide  
136 length  $L$ , because the surfaces are homogeneous. For the extra force  $F_e$ , we use the subscript  
137 “e” for “extra” and presumably “electrostatic”. It may depend on velocity, slide length, and  
138 drop number  $n$ .

139 To obtain the reference force, we assume that on Si wafers electrostatic forces are negligible.  
140 This assumption is in line with the fact that no differences in velocity were observed between  
141 successive drops (Figure 3A). With Eq. (4) we obtain  $F_r = mg \sin \alpha - m^* \frac{dU}{dt}$ . The acceleration  
142 is obtained from the measured velocity traces,  $U(t)$ . Due to noise, the measured  $U(t)$  curves  
143 were either smoothed before differentiation or the whole curve was fitted by a 1<sup>st</sup> to 4<sup>th</sup>  
144 order polynomial and the derivative of that polynomial was inserted. The reference forces  
145 increase linearly in the velocity range up to 0.4 m/s (Figure 3B). The increase is correlated with  
146 an increase in length and decrease in width of the drops (SI7).

147 By inserting the respective drop widths, advancing, and receding contact angles into Eq. (1)  
148 we calculated the capillary force with  $k = 1$  (Figure S6, red symbols). Capillary forces, which  
149 include wedge viscous forces (SI1) make up for most of the measured reference forces (Figure  
150 S6, black symbols). Bulk viscous forces calculated with Eq. (2) (Figure S6, blue symbols)  
151 contribute less than 10% to the reference force (details in S8).

152 With the reference force  $F_r(U)$  obtained from experiments on Si wafers, we use  $U(t)$  curves  
153 measured on SiO<sub>2</sub> to calculate the extra force with Eq. (4)  $F_e^n = mg \sin \alpha - m^* \frac{dU}{dt} - F_r$  (Figure  
154 3C, SI9). These extra forces are significant, they depend on drop number, and they show a  
155 complex distance dependency. Usually, the 1<sup>st</sup> and 2<sup>nd</sup> drop experienced a strong force of 60-  
156 100  $\mu$ N (up to 50% of the reference force) which then decayed over the observation range of  
157 4 cm. The force is positive, hindering drop motion. After  $\approx 5$  drops the initially high, decaying  
158 force changed gradually to an initially low, increasing extra force. Drop 100 showed almost  
159 the inverted profile as the first drop: Starting around 30  $\mu$ N, it increased to typically 60  $\mu$ N  
160 after 4 cm slide length.

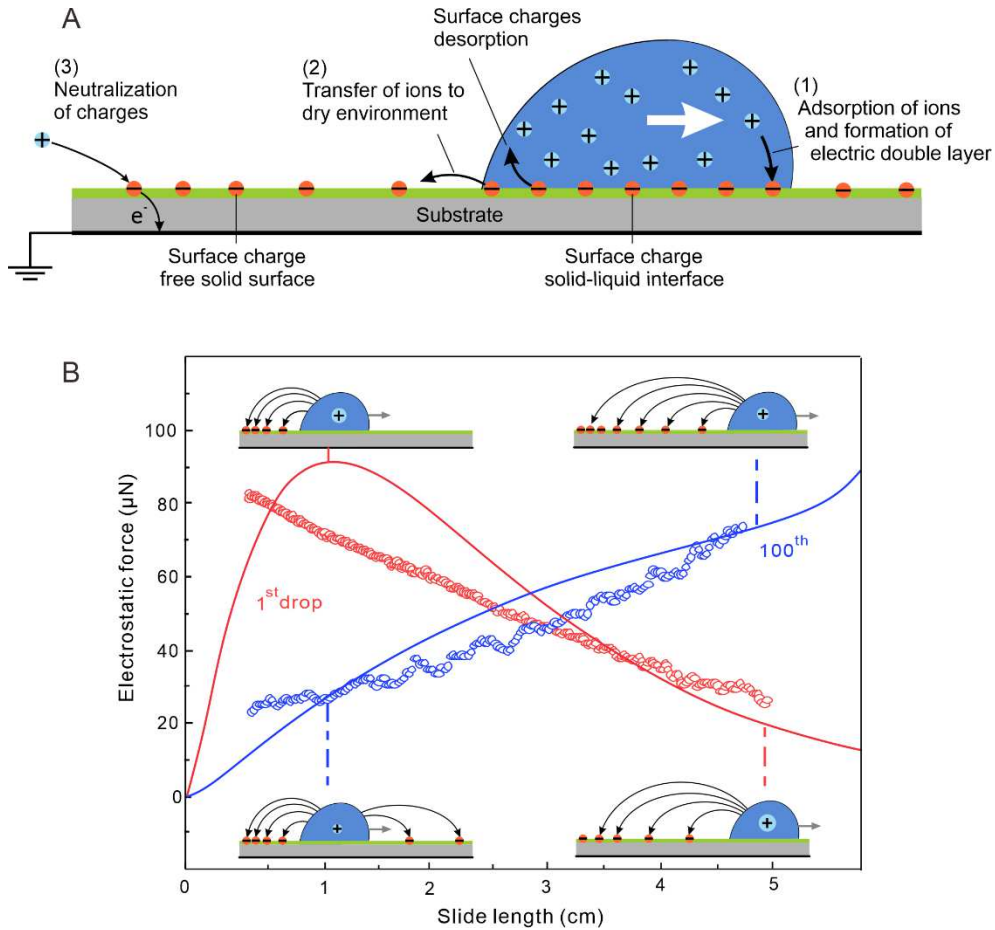
161 To determine the origin of the extra force, we measured drop charges (SI10). In agreement  
162 with earlier results <sup>35</sup>, on SiO<sub>2</sub> substrates drops gained a positive charge and leave behind a  
163 negative surface charge. For the first drop the charge was typically  $Q_1 = 1.0 - 1.5$  nC on 1  
164 and 5 mm SiO<sub>2</sub> (Figure 3D, Table S2). It decreased with subsequent drops until it reached a  
165 saturation value of the order of 0.4 nC. In contrast, on silicon wafers drop charges were  
166 typically 5-10 times lower.

167 To explain the shapes and the magnitudes of the measured extra force, we calculate the  
 168 electrostatic force. Therefore, we derive the electric field by integrating the field strength as  
 169 given by Eq. (3) for the surface charge density  $\sigma_n(x)$ . Then we multiply it with the drop charge  
 170  $Q_n(x)$  to obtain the electrostatic force:

$$171 \quad F_e^n(L) = -\frac{wQ_n(L)}{2\pi\epsilon_0(\epsilon_S+1)} \left( \int_0^L \frac{\sigma_n(x)}{(L+a-x)^2} dx - \int_{L+l}^{L_{end}} \frac{\sigma_{n-1}(x)}{(x-L-a)^2} dx \right). \quad (5)$$

172 Here,  $x$  is a coordinate along the path of the drop itself and the path of previous drops. The  
 173 first integral represents the interaction of the drop with the surface charge distribution left  
 174 behind by itself. The second integral is due to the interaction with charges deposited by  
 175 previous drops ahead of the drop. Details are in SI11. The parameter  $a$  characterises the  
 176 position of the center of charge of the drop; it is the horizontal distance to the rear rim (Figure  
 177 S10). Its value was obtained from numerical calculations of the electric field distribution and  
 178 the electrostatic force (SI13).

179 We use a previously derived model to obtain plausible expressions for  $\sigma_n(x)$  and  $Q_n(x)$  <sup>35</sup>.  
 180 Briefly, surface charges behind a sliding drop are remnants of interfacial charges generated at  
 181 the water-solid interface <sup>11,14,33,41</sup> (Fig. 4A). Hydrophobic surfaces usually charge negatively in  
 182 water, probably by the adsorption of hydroxyl ions. Part of these charges fail to neutralise at  
 183 the rear of the sliding drop and remain on the surface. As a result, the drop becomes positively  
 184 charged. However, the transfer of charges to the solid-air surface decreases with increasing  
 185 drop potential <sup>35</sup>. As a result, the density of deposited surface charges decreases with distance:  
 186  $\sigma_1 = \sigma_0 e^{-x/\lambda}$ . Here,  $\sigma_0$  is the initial surface charge density and  $\lambda$  is a decay length (SI12). In  
 187 addition, we allow neutralization of surface charges. It is not yet clear which processes  
 188 dominate surface neutralization, e.g., flow of electrons through the grounded substrate or via  
 189 the surface, by ions in the air, or the ejection of electrons <sup>11,38</sup>. Neutralization is characterized  
 190 by an exponential process with a relaxation time constant  $\tau$  of typically 10 s. Based on the  
 191 independent parameters  $\sigma_0$ ,  $\lambda$ , and  $\tau$  (Table S2), the surface charge density is a function of the  
 192 position on the surface and the drop number.



193

194 **Figure 4.** (A) Model applied to calculate electrostatic forces-versus-slide length for series of  
 195 drops. Step (1): Surface charges are generated when water gets into contact with the surface  
 196 at the front of the drop, e.g., by the adsorption of  $\text{OH}^-$  leaving  $\text{H}_3\text{O}^+$  in solution. Step (2): At the  
 197 rear side of the drop, most surface charges are neutralized, e.g., by desorption of  $\text{OH}^-$ . A  
 198 fraction of surface charges, however, transfers to the solid-air interface. Step (3): Charges are  
 199 neutralized. (B) Calculated electrostatic force acting on the first drop (red line, eq. S14) and  
 200 after a large number of drops (blue line, eq. S21). For comparison, we plotted the experimental  
 201 results (symbols) for the first and 100<sup>th</sup> drop sliding down PFOTS-on-5mm- $\text{SiO}_2$  from figure 3C.  
 202 The parameters were chosen as determined from the measurements of drops charges (Table  
 203 S2,  $\sigma_0=2 \times 10^{-5} \mu\text{C}/\text{m}^2$ ,  $\lambda=1.5 \text{ cm}$ ,  $\tau=7 \text{ s}$ ), the experimental conditions ( $w=4 \text{ mm}$ ,  $l=5 \text{ mm}$ ,  $\Delta t=1.3$   
 204  $\text{s}$ ,  $L_{\text{end}}=6 \text{ cm}$ ), and the numerical computations for 5 mm thick substrates ( $a=1 \text{ mm}=0.2l$ , details  
 205 in S112).

206 Using Eq. (5) we obtain an analytic expression for the electrostatic force on the first drop (Eq.  
 207 S14) and for high drop numbers ( $n \rightarrow \infty$ , Eq. S21). The calculated electrostatic force yields the  
 208 same order of magnitude as the experimental results (Figure 4B) and it explains the observed  
 209 flip in the slope of  $F_e$ -versus- $L$  curves when going from the first to later drops with  $n \geq 10$ .

210 All drops start with zero charge and thus zero electrostatic force. The first drop deposits  
 211 negative charge on the neutral surface and acquires a positive charge within a distance of  $L \approx$   
 212  $\lambda$  (schematic top left Figure 4B). The increase of drop and surface charge leads to a steep

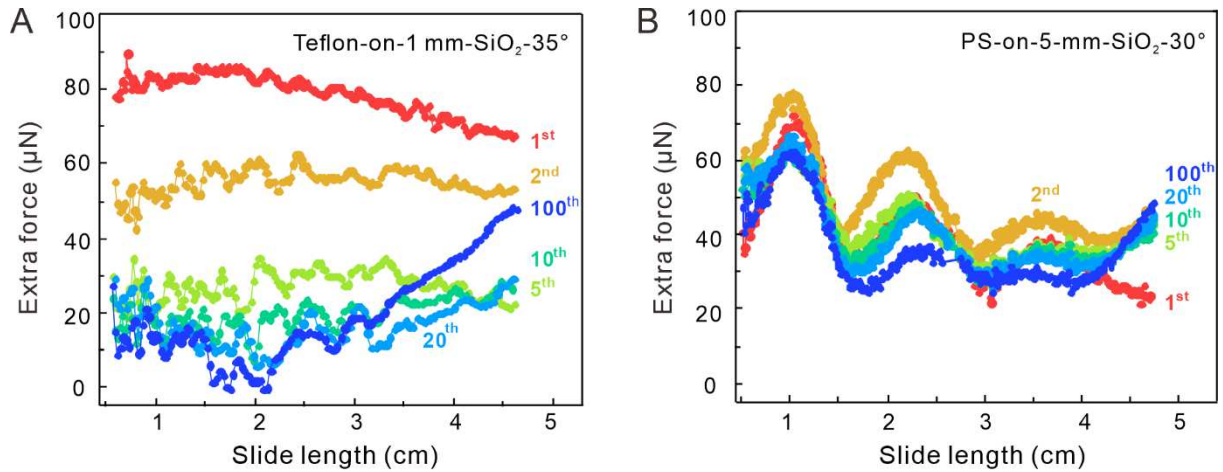
213 increase of the retarding electrostatic force with a peak at  $L \approx 0.8\lambda$ . As a result of drop  
214 charging, the drop potential increases which hinders further charge deposition and the drop  
215 charge saturates. As the drop reaches saturation and moves further from the strongly-charged  
216 region of the surface, the retarding electrostatic force decreases (bottom right).

217 The maximum predicted by the analytical solution at the beginning was missing in the  
218 experiments (Figure 4B, red symbols). This could be the effect of additional negative surface  
219 charge deposited right after the drop has impacted the surface before touching the first  
220 grounded electrode. As a result, a maximum would be outside our observation range. It was  
221 observed on other substrates described below.

222 For high drop number (blue line in Figure 4B, Figure S11), the electrostatic retardation  
223 increases with slide distance because of two effects. First, the surface charge density is already  
224 high from previous drops. As a result, the drop needs to cover a larger distance to reach its  
225 saturation charge (Figure 4B, top right). Second, the surface charges in front of the drop that  
226 are left behind by previous drops lead to an acceleration. At the end of its path, the  
227 electrostatic force increases even more steeply because there are no more attractive charges  
228 ahead since the sample ends.

229 The good agreement between experiment and electrostatic theory indicates that on PFOTS-  
230 coated insulators, the extra forces are predominantly caused by electrostatic charging. To find  
231 out how ubiquitous electrostatic forces are, we performed drop race experiments on other  
232 hydrophobic samples. When using conductive substrates or substrates with high permittivity  
233 (PS-on-gold, Teflon-on-gold, PDMS-on-Si, Thiols-on-gold) the first, second, and subsequent  
234 drops showed similar velocity profiles (Figure S15). Thus, electrostatic effects are negligible.  
235 In contrast, on 1 mm and 5 mm thick  $\text{SiO}_2$  coated with PS, Teflon, or PDMS velocity profiles of  
236 the first, second, and subsequent drops were distinctly different (Figure S16). This observation  
237 indicates, that drop motion is significantly influenced by electrostatic forces. Indeed, charging  
238 of drops was detected on PS, Teflon, and PDMS on  $\text{SiO}_2$  (Figure S9). In contrast, for PS-on-gold,  
239 Teflon-on-gold, and PDMS-on-Si, charging was at least ten times lower.

240 A complex variety of  $F_e^n$ -vs- $L$  graphs were observed, depending on drop number, tilt angle,  
241 and substrate thickness. Two typical examples are plotted in figure 5; a full set of results is  
242 shown in supporting information (Figure S18-20). On several samples, such as with Teflon-on-  
243 1mm- $\text{SiO}_2$ , we observed the maximum in the force-vs-slide length curves predicted by the  
244 electrostatic theory for the first drop (Figure 5A). We assume that a slight increase of the decay  
245 length  $\lambda$  shifts the maximum into our observation window. Charge measurements confirmed  
246 that indeed on Teflon,  $\lambda = 2.5$  cm rather than 1.5 cm as on PFOTS (Table S2). For higher drop  
247 number the maximum became weaker and for drop number  $n \geq 10$  an increasing extra force  
248 started to dominate at large slide lengths, in agreement with Eq. (S21).



249

250 **Figure 5.** Examples of extra forces acting on water drops sliding down (A) Teflon-on-1mm-SiO<sub>2</sub>  
 251 at 35° tilt and (B) PS-on-5mm-SiO<sub>2</sub> at 30° tilt. Plotted are results for the 1<sup>st</sup>, 2<sup>nd</sup>, 5<sup>th</sup>, 10<sup>th</sup>, 20<sup>th</sup>,  
 252 and the 100<sup>th</sup> drop. Extra forces were calculated with Eq. (4) and  $F_r = 48 \mu\text{N} + 175 \frac{\mu\text{Ns}}{\text{m}} \cdot U$   
 253 obtained with Teflon-on-gold and  $F_r = 74 \mu\text{N} + 398 \frac{\mu\text{Ns}}{\text{m}} \cdot U$  measured on PS-on-gold as  
 254 reference forces (Fig. S17).

255 Figure 5A, however, also shows limits of the simple model. It does not predict the minimum  
 256 in the electrostatic force for  $n \geq 10$  at short slight lengths. This deficit could be caused by the  
 257 assumption, that charge deposition depends on slide velocity. Since deposition of charges is a  
 258 non-equilibrium process, it will most likely depend on the velocity. At low velocity, charge  
 259 deposition is probably less pronounced than assumed. A velocity dependence of charge  
 260 deposition is most likely also the reason for the oscillating electrostatic forces observed e.g.,  
 261 on PS-on-5mm-SiO<sub>2</sub>. (Figure 5B). The oscillation period was not related to drop vibrations,  
 262 which were at 50 Hz or faster. Thus, a future refinement of the description of charge  
 263 deposition needs to include the velocity of the receding contact line.

264 In summary, electrostatic forces significantly influence drop motion on hydrophobic, low-  
 265 permittivity surfaces. They depend on slide distance, drop number, and the particular surface  
 266 coating. While static shape of drops is largely determined by the surface molecules, the  
 267 dynamics of drops is strongly influenced by the substrate down to a depth of millimetres. The  
 268 mobility of water drops on hydrophobic surfaces can be increased by using conductive or high-  
 269 permittivity substrates. Accordingly, the fastest drops in our “race court” were on the  
 270 Perfluorodecanethiol -coated gold and Teflon films on gold (Figure 1E, F).

## 271 Methods

### 272 Tilted plate experiments

273 To measure forces acting on sliding drops, 33 μL water drops were deposited at intervals of  
 274 1.3 s at the top of a tilted sample by a grounded syringe needle (Hamilton, 2 mm diameter),  
 275 which was connected to a peristaltic pump (Minipuls 3, Gilson) (Figure S11). Before every series

276 of drops, surfaces were neutralized by an ionizing air blower for 10 min (Aerostat PC Ionizing  
277 Air Blower, Simco-Ion). Drops fell  $\approx 5$  mm, just enough so that they detached from the syringe  
278 before touching the surface. To make sure drops start sliding without initial charge they were  
279 neutralized by a 0.025 mm diameter grounded tungsten wire, right after they landed on the  
280 surface. The position where the drops detach from the grounded wire corresponds to slide  
281 length zero ( $L = 0$ ). The observation range starts where the full drop has detached from the  
282 grounded wire and the wire is not in the image anymore; that is at  $L = 0.5$  cm. Then we  
283 imaged the drop with a frame rate of 1000 fps in side and front view over a length of typically  
284 4.5 cm with a high-speed camera (FASTCAM MINI UX100, Photron with a Titan TL telecentric  
285 lens,  $0.268\times$ , 1" C-Mount, Edmund Optics). By applying two parallel mirrors (25 mm x 36 mm  
286 protected silver mirror, PFR10-P01, THOPLABS) at both sides of the sample to guide the  
287 backlight from the telecentric backlight illuminator (138 mm, Edmund Optics), we also imaged  
288 the front view of sliding drops at the same time. After typically  $L_{end} = 6$  cm the rim of the  
289 sample was reached and the drops fell off. To access a wide velocity range, we varied the tilt  
290 angle (Fig. S3A). On longer samples we verified that, after a slide length of  $\approx 10 - 15$  cm,  
291 drops reach a steady state velocity (Fig. S3B). From video images we extract the slide length  
292  $L$ , the velocity of the drop  $U$ , the contact angles at the front (advancing contact angle  $\Theta_a$ ) and  
293 the rear (receding contact angle  $\Theta_r$ ), the length, and the width of the drop. All parameters  
294 vary with time and thus with position. To extract  $\Theta_a(U)$  and  $\Theta_r(U)$  from the videos, we  
295 adapted the open drop shape analysis from MATLAB (DSaFM). Dynamic contact angles were  
296 determined by applying a polynomial fit to every contour image. More details are in  
297 supporting information SI2.

## 298 **Sample preparation**

299 Five types of surfaces were prepared: (1) **Perfluorooctadecyltrichlorosilane (PFOTS)**  
300 **monolayers** on Si wafer, 1 mm and 5 mm thick SiO<sub>2</sub> slides were prepared by chemical vapor  
301 deposition. After O<sub>2</sub> plasma cleaning at 300 W for 10 min (Femto low-pressure plasma system,  
302 Diener electronic), the Si wafer ( $1.6\pm 0.3$  nm native oxide layer as measured by ellipsometry,  
303 resistivity  $< 0.005$   $\Omega$ cm, thickness  $525\pm 25$   $\mu$ m, Silicon Materials) and the SiO<sub>2</sub> slides were  
304 placed in a vacuum desiccator containing a vial with 0.5 mL of 1H,1H,2H,2H-perfluoro-  
305 octadecyltrichlorosilane (97%, Sigma Aldrich). We used 1 mm thick SiO<sub>2</sub> slides ( $76.2\times 25.4\times 1$   
306 mm<sup>3</sup>, Thermo Fisher Scientific) and 5 mm thick SiO<sub>2</sub> slides ( $75\times 25\times 5$  mm<sup>3</sup>, Präzisions Glas &  
307 Optik GmbH). The desiccator was evacuated to less than 100 mbar, closed and the reaction  
308 was allowed to proceed for 30 min. (2) **Polystyrene (PS) films** on gold, 1 mm and 5 mm thick  
309 SiO<sub>2</sub> slides were prepared by dip coating. To get gold substrates, 30 nm gold was sputtered  
310 onto  $75\times 25$  mm<sup>2</sup> glass slides that had been pre-coated with 5 nm chromium to improve  
311 adhesion. The solution consisted of 1 wt% PS ( $M_w = 192$  kg/mol, Sigma Aldrich) in toluene.  
312 After moving down the substrates with a speed of 90 mm/min into the solution and waiting  
313 for 10 s, the substrates were moved up again with a speed of 90 mm/min. Finally, the films  
314 were annealed in an oven at 120°C under vacuum for 24 h. PS films were 20 nm thick measured  
315 by a profiler (P-7 Stylus Profiler, KLA-Tencor). (3) **Teflon AF1600 (Teflon) films** on gold, 1 mm

316 and 5 mm thick SiO<sub>2</sub> slides were also prepared by dip coating. Sputter-coated gold glass slides  
317 (see above) or the SiO<sub>2</sub> slides were immersed into 1 wt% Teflon AF1600 (Sigma Aldrich) in FC-  
318 43 (Sigma Aldrich) with a speed of 90 mm/min. After being immersed for 10 seconds, the  
319 substrates were withdrawn from the solution at a constant speed of 10 mm/min. Finally, the  
320 films on the substrates were annealed at 160°C in vacuum for 24 h. Teflon AF1600 films were  
321 60 nm thick to avoid dewetting. (4) **Polydimethylsiloxanes (PDMS) polymer brushes** on Si  
322 wafers, 1 mm and 5 mm thick SiO<sub>2</sub> slides were prepared as described in <sup>42</sup>. After O<sub>2</sub> plasma  
323 cleaning (see above), few PDMS drops (*M<sub>w</sub>*=6 kg/mol, Alfa Aesar) were deposited on the Si  
324 wafer or SiO<sub>2</sub>. After the PDMS drop spread and covered the substrates, the samples were kept  
325 at 22–23°C and 30–60% relative humidity for 24–48 h. Then they were rinsed with toluene and  
326 sonicated in toluene, ethanol, and DI water for 10 min each, to wash away unbound PDMS.  
327 Brushes were ≈3 nm thick <sup>42</sup>. (5) **1H,1H,2H,2H-Perfluorodecanethiol (Thiols) monolayers on**  
328 **gold**. Directly after preparation of gold-coated glass slide (see above) the surfaces were  
329 immersed in 1 mM ethanolic thiol (≥96.0%, Sigma Aldrich) solution for 24 h. Then the surfaces  
330 were rinsed by pure ethanol and dried by Ar<sub>2</sub> blowing.

### 331 **Scanning force microscope imaging**

332 All hydrophobic surfaces were studied with scanning force microscopy (Dimension Icon,  
333 Bruker) in tapping mode (Figure S2). SFM tips with a nominal resonance frequency of 300 kHz  
334 and a spring constant of 26 N/m were used (160AC-NA, OPUS). The root mean square  
335 roughness (rms) was determined over 0.5×0.5 μm<sup>2</sup> for each sample. The error was roughly 0.1  
336 nm, except for the thiols on gold and PFOTS, where it was 0.2 nm. Errors were determined  
337 from variations observed at different positions on samples and variations on different samples.

### 338 **Static contact angle measurements**

339 “Static” advancing and receding contact angles  $\theta_a^0$  and  $\theta_r^0$  were measured with sessile water  
340 drops (Contact angle measurement system, OCA35, Dataphysics). An 8 μL water drop was  
341 deposited on the surface. Then 16 μL of DI water was pumped into the drop and subsequently  
342 sucked out at a rate of 0.5 μL/s by a Hamilton syringe connected to a hydrophobic needle. The  
343 process was repeated three times without interruption. During inflation and deflation, drops  
344 were imaged in side view.  $\theta_a^0$  and  $\theta_r^0$  were calculated by fitting an ellipse model to the contour  
345 images. Error: ±2°.

### 346 **Acknowledgements**

347 We thank Zuankai Wang, Hong Kong, and Robin Ras, Aalto, for critically reading the  
348 manuscript. The research leading to these results has received funding from the European  
349 Research Council under the European Union's Seventh Framework Programme (FP7/2007-  
350 2013)/ERC grant agreement n°883632 (A.S., H.B., H.J.B., P.B.). We further acknowledge  
351 financial support by the German Research Society via the CRC 1194 Interaction between  
352 Transport and Wetting Processes (F.B., H.J.B., H.M., S.H.) and the Priority Programme 2171  
353 Dynamic wetting of flexible, adaptive and switchable surfaces (H.J.B., R.B., X.L.).

354 **Author contributions**

355 Xiaomei Li carried prepared the samples, performed the tilted plate experiments and analysed  
356 the data. Xiaomei Li, Alexander Saal and Rüdiger Berger designed the tilted plate setup.  
357 Pravash Bista, Amy Stetten and Stefan Weber measured drop charges. Henning Bonart  
358 numerically calculated the electrostatic force on a drop. Francisco Bodziony and Holger  
359 Marschall carried out the numerical diffuse interface simulations of drop motion. Alexander  
360 Saal. Stefan Weber, Steffen Hardt, Maximilian T. Schür, Hans-Jürgen Butt derived the  
361 analytical theory. Hans-Jürgen Butt derived the concept of extracting the electrostatic force  
362 from the equation of motion. All authors discussed and interpreted the results and wrote the  
363 manuscript.

364 **Competing financial interests**

365 The authors declare no competing financial interests.

366

## 367 References

- 368 1 de Gennes, P. G. Wetting: Statics and dynamics. *Rev. Modern Phys.* **57**, 827-863 (1985).
- 369 2 Starov, V. M., Velarde, M. G. & Radke, C. J. *Wetting and Spreading Dynamics*. (CRC  
370 Press, 2007).
- 371 3 Bonn, D., Eggers, J., Indekeu, J., Meunier, J. & Rolley, E. Wetting and spreading. *Rev.*  
372 *Modern Physics* **81**, 739-805 (2009).
- 373 4 Tuteja, A. *et al.* Designing superoleophobic surfaces. *Science* **318**, 1618-1622 (2007).
- 374 5 Wang, L. M. & McCarthy, T. J. Covalently attached liquids: Instant omniphobic surfaces  
375 with unprecedented repellency. *Angew. Chem. Int. Ed.* **55**, 244-248 (2016).
- 376 6 Huhtamaki, T., Tian, X. L., Korhonen, J. T. & Ras, R. H. A. Surface-wetting  
377 characterization using contact-angle measurements. *Nature Protocols* **13**, 1521-1538  
378 (2018).
- 379 7 Tadmor, R. Open problems in wetting phenomena: Pinning retention forces. *Langmuir*  
380 **37**, 6357-6372 (2021).
- 381 8 Gao, N. *et al.* How drops start sliding over solid surfaces. *Nature Physics* **14**, 191 (2017).
- 382 9 Backholm, M. *et al.* Water droplet friction and rolling dynamics on superhydrophobic  
383 surfaces. *Nature Communications Materials* **1**, 64 (2020).
- 384 10 Lin, Z. H., Cheng, G., Lee, S., Pradel, K. C. & Wang, Z. L. Harvesting water drop energy  
385 by a sequential contact-electrification and electrostatic-induction process. *Adv. Mater.*  
386 **26**, 4690-4696 (2014).
- 387 11 Sun, Y. J., Huang, X. & Soh, S. Using the gravitational energy of water to generate power  
388 by separation of charge at interfaces. *Chemical Science* **6**, 3347-3353 (2015).
- 389 12 Park, J. *et al.* Identification of droplet-flow-induced electric energy on electrolyte-  
390 insulator-semiconductor structure. *J. Am. Chem. Soc.* **139**, 10968-10971 (2017).
- 391 13 Boamah, M. D. *et al.* Energy conversion via metal nanolayers. *Proc. Natl. Acad. Sci. USA*  
392 **116**, 16210-16215 (2019).
- 393 14 Helseth, L. E. A water droplet-powered sensor based on charge transfer to a flow-  
394 through front surface electrode. *Nano Energy* **73**, 104809 (2020).
- 395 15 Xu, W. H. *et al.* A droplet-based electricity generator with high instantaneous power  
396 density. *Nature* **578**, 392-396 (2020).
- 397 16 Wu, H., Mendel, N., van den Ende, D., Zhou, G. F. & Mugele, F. Energy harvesting from  
398 drops impacting onto charged surfaces. *Phys. Rev. Lett.* **125**, 078301 (2020).
- 399 17 Wang, K. Q. & Li, J. J. Electricity generation from the interaction of liquid-solid  
400 interface: a review. *J. Mater. Chem. A* **9**, 8870-8895 (2021).
- 401 18 Suzuki, S., Nakajima, A., Kameshima, Y. & Okada, K. Elongation and contraction of  
402 water droplet during sliding on the silicon surface treated by fluoroalkylsilane. *Surf.*  
403 *Sci.* **557**, L163-L168 (2004).
- 404 19 Snoeijer, J. H. & Andreotti, B. Moving contact lines: Scales, regimes, and dynamical  
405 transitions. *Ann. Rev. Fluid Mech.* **45**, 269-292 (2013).

- 406 20 Olin, P., Lindstrom, S. B., Pettersson, T. & Wagberg, L. Water drop friction on  
407 superhydrophobic surfaces. *Langmuir* **29**, 9079-9089 (2013).
- 408 21 Furmidge, C. G. L. Studies at phase interfaces. I. The sliding of liquid drops on solid  
409 surfaces and a theory for spray retention. *J. Colloid Sci.* **17**, 309-324 (1962).
- 410 22 Wolfram, E. & Faust, R. in *Wetting, Spreading and Adhesion* (ed J.F. Padday) 213-222  
411 (Academic Press, 1978).
- 412 23 Extrand, C. W. & Kumagai, Y. Liquid drops on an inclined plane: The relation between  
413 contact angles, drops hape, and retention forces. *J. Colloid Interface Sci.* **170**, 515-521  
414 (1995).
- 415 24 Kim, H. Y., Lee, H. J. & Kang, B. H. Sliding of liquid drops down an inclined solid surface.  
416 *J. Colloid Interface Sci.* **247**, 372-380 (2002).
- 417 25 Marsh, J. A., Garoff, S. & Dussan, E. B. Dynamic contact angles and hydrodynamics near  
418 a moving contact line. *Phys. Rev. Lett.* **70**, 2778-2781 (1993).
- 419 26 Le Grand, N., Daerr, A. & Limat, L. Shape and motion of drops sliding down an inclined  
420 plane. *J. Fluid Mech.* **541**, 293-315 (2005).
- 421 27 Macdougall, G. & Ockrent, C. Surface energy relations in liquid/solid systems. I. The  
422 adhesion of liquids to solids and a new method of determining the surface tension of  
423 liquids. *Proc. Roy. Soc. London A* **180**, 151-173 (1942).
- 424 28 Dimitrakopoulos, P. & Higdon, J. J. L. On the gravitational displacement of three-  
425 dimensional fluid droplets from inclined solid surfaces. *J. Fluid Mech.* **395**, 181-209  
426 (1999).
- 427 29 ElSherbini, A. & Jacobi, A. Retention forces and contact angles for critical liquid drops  
428 on non-horizontal surfaces. *J. Colloid Interface Sci.* **299**, 841-849 (2006).
- 429 30 Sakai, M. *et al.* Direct observation of internal fluidity in a water droplet during sliding  
430 on hydrophobic surfaces. *Langmuir* **22**, 4906-4909 (2006).
- 431 31 Richard, D. & Quéré, D. Viscous drops rolling on a tilted non-wettable solid. *Europhys.*  
432 *Lett.* **48**, 286-291 (1999).
- 433 32 Yilbas, B. S., Al-Sharafi, A., Ali, H. & Al-Aqeeli, N. Dynamics of a water droplet on a  
434 hydrophobic inclined surface: influence of droplet size and surface inclination angle on  
435 droplet rolling. *RSC Advances* **7**, 48806-48818 (2017).
- 436 33 Yatsuzuka, K., Mizuno, Y. & Asano, K. Electrification phenomena of pure water droplets  
437 dripping and sliding on a polymer surface. *J. Electrostatics* **32**, 157-171 (1994).
- 438 34 Shahzad, A., Wijewardhana, K. R. & Song, J. K. Contact electrification efficiency  
439 dependence on surface energy at the water-solid interface. *Appl. Phys. Lett.* **113**,  
440 023901 (2018).
- 441 35 Stetten, A. Z., Golovko, D. S., Weber, S. A. L. & Butt, H. J. Slide electrification: charging  
442 of surfaces by moving water drops. *Soft Matter* **15**, 8667-8679 (2019).
- 443 36 Sun, Q. *et al.* Surface charge printing for programmed droplet transport. *Nature*  
444 *Materials* **18**, 936-941 (2019).

- 445 37 Zhang, W. L., Sun, Q. Q., Butt, H. J., Wang, Z. K. & Deng, X. Surface charges as a versatile  
446 platform for emerging applications. *Science Bulletin* **65**, 1052-1054 (2020).
- 447 38 Lin, S. Q., Xu, L., Wang, A. C. & Wang, Z. L. Quantifying electron-transfer in liquid-solid  
448 contact electrification and the formation of electric double-layer. *Nature*  
449 *Communications* **11**, 399 (2020).
- 450 39 Yarnold, G. D. The motion of a mercury index in a capillary tube. *Proceedings of the*  
451 *Physical Society* **50**, 540-552 (1938).
- 452 40 Shikhmurzaev, Y. D. The moving contact line on a smooth solid surface. *Int. J.*  
453 *Multiphase Flow* **19**, 589-610 (1993).
- 454 41 Choi, D. *et al.* Spontaneous electrical charging of droplets by conventional pipetting.  
455 *Scientific Reports* **3**, 2037 (2013).
- 456 42 Teisala, H., Baumli, P., Weber, S. A. L., Vollmer, D. & Butt, H. J. Grafting silicone at room  
457 temperature - a transparent, scratch-resistant nonstick molecular coating. *Langmuir*  
458 **36**, 4416-4431 (2020).

459

## Supplementary Files

This is a list of supplementary files associated with this preprint. Click to download.

- [SupportingMaterials.pdf](#)